RESEARCH ARTICLE

WILEY

Experimental investigation and numerical modeling of rocking cross laminated timber walls on a flexible foundation

Sarah Wichman¹ Jeffrey W. Berman¹ Shiling Pei²

Correspondence

Sarah Wichman, Department of Civil and Environmental Engineering, University of Washington, Seattle, WA 98195, USA. Email: wichman@uw.edu

Abstract

With recent developments of engineered wood products such as cross laminated timber, mass timber buildings in areas of high seismicity are becoming feasible and offer benefits such as faster construction and unique architectural features. It has also opened the door to creating seismically resilient lateral systems that sustain minor and reparable damage during large earthquakes. This paper presents a numerical modeling procedure for mass timber rocking wall lateral system with distributed spring elements to model base rocking. This modeling technique was validated by comparing the behavior with results from the full-scale two-story shake table test on a mass timber building with coupled CLT rocking walls completed as part of the NHERI TallWood Project. Although the lateral system performed better than expected during testing, it was determined that the flexibility of the foundation actually limited damage to the rocking wall panels. By adjusting the numerical model to represent a rigid foundation boundary condition, it was determined that the wall system would have experienced more damage, but would have still met design performance objectives had it been tested on a rigid foundation.

KEYWORDS

cross laminated timber (CLT), numerical modeling, rocking walls, seismic performance, shake table testing

INTRODUCTION

Using mass timber rocking walls as the main lateral force resisting system in buildings located in areas of high seismicity is gaining interest with the increase in popularity of mass timber products. In mass timber rocking wall systems, unbonded post-tension (PT) connections are used for recentering purposes while energy dissipation devices (such as U-shaped flexural plates [UFP]) provide energy dissipation for the system. This results in an efficient structural system that can undergo large inelastic deformations while also recentering following large earthquakes. The design of the replaceable UFP components allows for predictable and localized yielding that can be easily repaired after large earthquake events. While this study focuses on CLT rocking walls, similar concepts and modeling approaches can be applied for other mass timber panel products such as mass plywood panels.

Mass timber rocking walls may be designed as seismically resilient systems that sustain minor, but easily repairable, damage during frequent earthquakes and achieve collapse prevention for maximum considered earthquake intensity.

¹Department of Civil and Environmental Engineering, University of Washington, Seattle, Washington, USA

²Department of Civil and Environmental Engineering, Colorado School of Mines, Golden, Colorado, USA

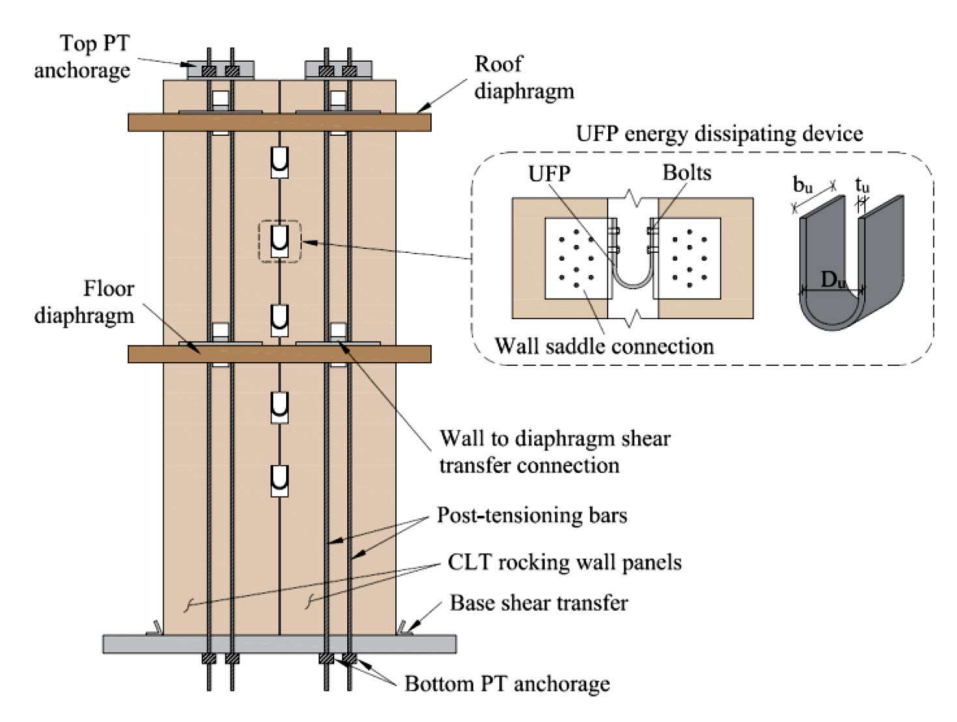


FIGURE 1 Coupled post-tensioned rocking wall schematic

These multiple performance goals are achieved by designing for rigorous performance objectives for different earthquake intensity levels and ensuring critical force and deformation limits are not exceeded for important components in the system such as the PT bars, the UFPs, and the mass timber walls themselves.

Various numerical modeling approaches have been proposed for post-tensioned rocking wall systems. For lumped plasticity models, such as those developed by Iqbal¹ and Sarti² for laminated veneer lumber (LVL) rocking walls and Pei et al.³ for CLT walls, a nonlinear rotational spring at the base of the wall panels model base rocking. While these models are efficient and can capture global behavior of the system well, they lack the ability to assess detailed behavior of the components such as damage to the wood at the base of the wall. Alternatively, distributed plasticity models utilize distributed springs in parallel at the base of the wall to model base rocking and compressive behavior of the wood at the base. While these models are typically less computationally efficient, they can provide detailed information about individual wall components. The distributed plasticity models proposed by Sarti² and Ganey⁴ were compared to experimental results on LVL and CLT rocking walls, respectively. Both models accurately captured system force-deformation behavior and provided valuable information about the compression neutral axis depth at the base of the wall and wall uplift that cannot be determined from lumped plasticity models.

To better understand the performance and behavior of using rocking mass timber walls as a seismic force resisting system, a full-scale two-story mass timber building with cross laminated timber (CLT) rocking walls was tested on the NHERI@UCSD (Natural Hazards Engineering Research Infrastructure) shake table at the University of California, San Diego as part of the NHERI TallWood Project. Figure 1 illustrates the post-tensioned coupled rocking wall system utilized in the test. As will be discussed, the specimen performed better than expected and the rocking walls met all design performance objectives. However, the foundation supporting the rocking walls was unexpectedly flexible and permanent deformations in the flange of the steel foundation beam were observed during even small hazard level earthquakes, altering the behavior of the structure, and resulting in less damage to the CLT wall than expected. Extending the results of these shake table tests thus requires numerical modeling to remove the foundation flexibility. While pervious publications have focused on the design and performance of the overall structure, 5,7 this paper focuses specifically on the design and performance of the CLT walls and will address the impact of the flexible foundation and predict the performance of the structure had the foundation been rigid.

A detailed numerical modeling technique using distributed springs to simulate the rocking interface is presented and validated using the results from the two-story shake table test. This model provides valuable information about individual wall components during dynamic response including the PT bars, UFPs, and damage to the base of the rocking wall at the corners. With this level of detail, the model is well suited to investigate the impact of the flexible foundation beam observed

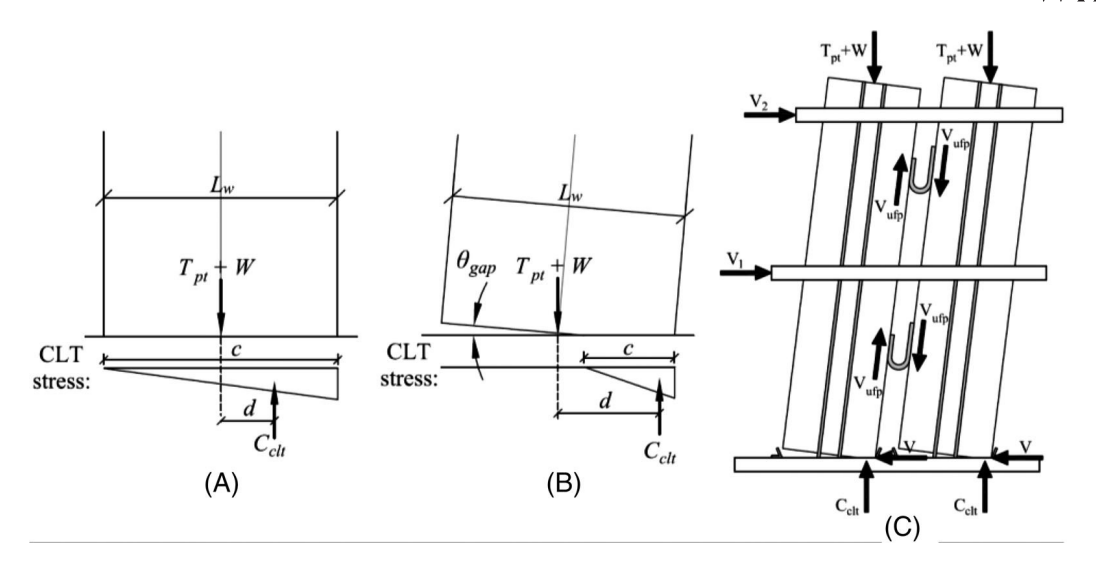


FIGURE 2 Rocking wall equilibrium: (A) CLT stress strain at base of wall at decompression, (B) CLT stress strain at base of wall after significant uplift, and (C) full rocking wall system behavior under lateral load

during the test. When comparing the numerical model with the experimental results, the contribution of the foundation flexibility was included in the model with additional springs at the foundation level. With modeling techniques validated, the foundation flexibility was removed from the model to predict how the test structure would have behaved with a rigid foundation since that is more likely to represent a realistic building. The response of the numerical model under rigid foundation boundary conditions was compared to design performance objectives and used to further determine the impact of the flexible foundation.

2 | BEHAVIOR OF ROCKING CLT WALLS

2.1 | Post-tensioned connections

In the rocking CLT wall considered here, the wall panels are precompressed against the foundation using unbonded steel post-tensioning bars, which are fixed to the foundation at the base of the wall and anchored to the top of the wall. Apart from the post-tensioned bars, the wall is not otherwise attached directly to the foundation; however, some form of shear transfer is needed at the base to prevent sliding. Once lateral loads produce a moment that exceeds the decompression moment, a gap opens at the base of the wall. Prior to decompression, the overturning moment is resisted by the initial PT force, $T_{o,pt}$, and gravity loads, W, and behaves as a cantilever such that displacements are a result of shear and flexural deformations, and not rigid body rotation. Assuming a linear distribution of the CLT compression stress along the base of the wall, as shown in Figure 2A, the decompression moment can be approximated as:

$$M_{dec} = \left(T_{o,pt} + W\right)d\tag{1}$$

where d is the distance between the resisting CLT panel compression force, C_{clt} , and the resultant of the initial PT force and the gravity load. The resultant of the CLT compression stress acts at the centroid of its triangular distribution. If the resultant of the initial PT force and gravity load acts through the wall's centroid at $L_w/2$, where L_w is the length of the wall, then the moment arm, d, is $L_w/6$ at the decompression moment.

After decompression, a gap, θ_{gap} , opens between the wall base and the foundation. However, the lateral-load response is essentially linear-elastic until the portion of the wall base in compression and in contact with the foundation, c, is at least less than $L_w/2$ and the PT bars begin to elongate. Figure 2B shows the stress distribution at the base of the wall when the contact length is less than $L_w/2$. Akbas et al. 8 defines an effective linear limit (ELL) which corresponds to a visible gap and reduced contact length such that the lateral stiffness of the wall is reduced enough to exhibit significant nonlinear behavior. This point is assumed to occur when the contact length, c, is approximately $3L_w/8$ and the elongation of the PT is assumed negligible. The contact length is based on fit to experimental results from Ganey⁴ and was proposed by Akbas

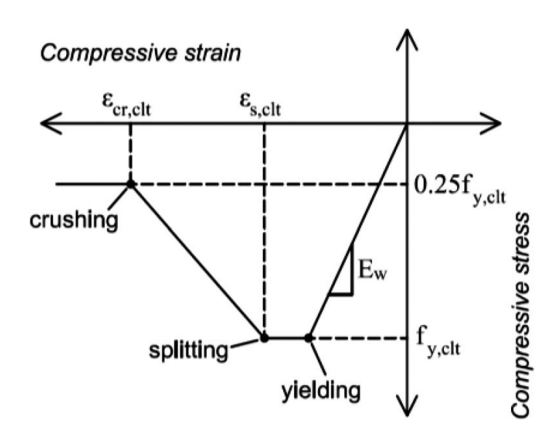


FIGURE 3 Idealized compressive stress strain relationship for CLT material

et al. Similar to Equation (1), M_{ell} can be calculated assuming initial PT force, $T_{o,pt}$, and a linear stress distribution along the contact length, resulting in a moment arm, d, also equal to $3L_w/8$.

UFPs are assumed to remain elastic and do not contribute significantly to moment resistance until after the decompression moment, but before the ELL. Once the UFPs experience significant deformations, they will yield and produce a shear force, V_{ufp} , along the vertical edge of the wall. Figure 2C shows a free body diagram of coupled post-tensioned rocking walls at a point beyond decompression, with the contribution of the UFPs.

Although, the moment in the two walls will differ because of the UFP forces, the difference is assumed negligible because the force in the PT bars is much greater than the vertical force provided by the UFPs. Thus, equal base moment in each wall panel is assumed. As a result, the total moment at the base of the wall system, after UFP yielding, can be calculated as:

$$M = \sum_{1}^{n_s} V_i h_i = n_p (T_{pt} + W) d + n_{ufp} (V_{ufp} L_w)$$
 (2)

where n_s is the total number of stories, n_p is the total number of panels in the wall, T_{pt} is the total force in the bars after elongation, and n_{upf} is the number of UFPs. As the panels rock and the CLT deforms, the portion of the wall base in compression changes constantly. As long as the peak stress at the base of the CLT wall remains below yield, the stress distribution will be linear. During uplift, as the lateral load increases, the PT bars stretch, increasing their tension force and the resisting moment. The UFPs also deform, further increasing the resisting moment. As long as the PT bars remain elastic, they will shorten upon unloading and the initial PT force will fully recenter the walls.

2.2 UFP energy dissipating devices

UFPs can be used as the primary source of energy dissipation when mounted between two rocking CLT wall panels as shown in Figure 1. The UFP dissipates energy when one end of the UFP moves relative to the other end, yielding the steel back and forth along the plate. Bolted saddle connections, like the one shown in Figure 1 make for easy replacement of damaged UFPs after large seismic events. Figure 1 also shows a schematic of a typical UFP, where t_u is the thickness of the plate, b_u is the width of the UFP, and D_u is the diameter of the UFP.

2.3 | CLT wall panel behavior

For this study, the stress-strain behavior of CLT is based on compression tests completed on 5-ply, E2-M1, DR Johnson CLT at Oregon State University. As shown in Figure 3, in compression, the behavior can be approximated as elastic, with an elastic modulus of E_w , until the yield stress, $f_{y,clt}$ is reached. After yielding, the behavior can be approximated with a zero strain-hardening plateau until CLT splitting begins at the splitting strain, $\varepsilon_{s,clt}$. After splitting, the strength deteriorates until crushing occurs at approximately 25% of the yield stress and at the crushing strain, $\varepsilon_{cr,clt}$.

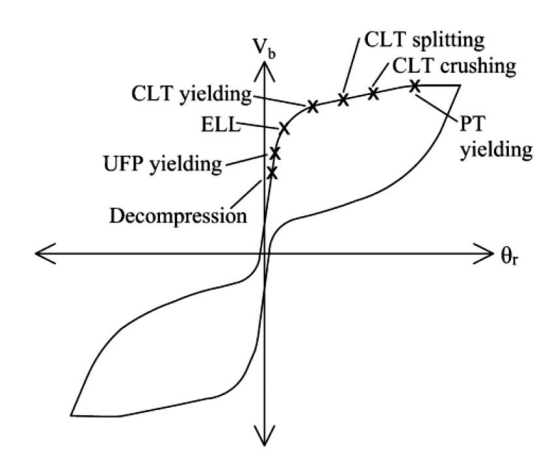


FIGURE 4 Hysteretic behavior of rocking CLT wall systems

2.4 | Cyclic behavior

The PT bars, in combination with gap opening at the base of the wall, provide a nonlinear elastic response with zero residual rotation after unloading. However, with only PT bars, the system lacks damping. The hysteretic behavior of the steel yielding energy dissipaters provides the needed energy dissipation. The combination of the unbonded PT bars and the energy dissipaters produces a hybrid system that can undergo large inelastic deformations while assuring recentering and minimized damage. The resulting flag shaped hysteresis is shown in Figure 4.

Figure 4 also shows structural limit states defined in previous research by Akbas et al.⁸ and Ganey et al.¹¹ Under small lateral forces, prior to decompression, the wall remains linear and elastic with a stiffness equal to the elastic shear and flexural stiffness of the CLT panels alone. After the decompression point, the stiffness decreases slightly. Notable nonlinearity occurs after significant uplift occurs; this point is defined as the ELL. The UPFs will yield in the region between the decompression point and the ELL or just after the ELL depending on their strength and stiffness. With increasing lateral displacement, significant uplift and nonlinear behavior begins. The system is designed such that the base of the CLT panels will yield, split, and crush (as shown in Figure 3) prior to PT yielding.

3 | SUMMARY OF TEST SPECIMEN DESIGN

To better understand the seismic performance and behavior of mass timber rocking wall lateral systems, such as the ones described above, a full-scale two-story mass timber building was tested on the NHERI@UCSD shake table. Figure 5 shows a photo and schematic of the test specimen. To extend the usable width of the shake table and study diaphragm action, the gravity columns sat atop four steel gravity frame extender beams that cantilevered off the shake table (perpendicular to the direction of shaking). The seismic force resisting system, comprised of two coupled rocking CLT walls, was also placed atop steel foundation beams to make the entire structure start at the same elevation. This section will discuss the post-tensioned rocking walls in detail and presents the information pertinent to the design of the CLT wall system and the details necessary for the numerical models presented later. The design of the remaining structure will only be discussed briefly; more details on other aspects of the design can be found in Pei et al.⁵ and Barbosa et al.⁷

3.1 | Design loads

The building was designed assuming typical office loading with a dead load of 321 and 386 kg/m^2 on the floor and roof levels, respectively. Because nonstructural elements were not included on the test structure and because concrete was only added on the roof level, additional mass was added in the form of large steel trench plates to achieve the intended design seismic mass. Although the final weight of the structure was intended to be equivalent to the design dead load (329 kN on the floor level and 409 kN on the roof level), the actual seismic weight, not including the weight of the CLT walls themselves, was estimated as 391 and 400 kN for the floor and roof, respectively.

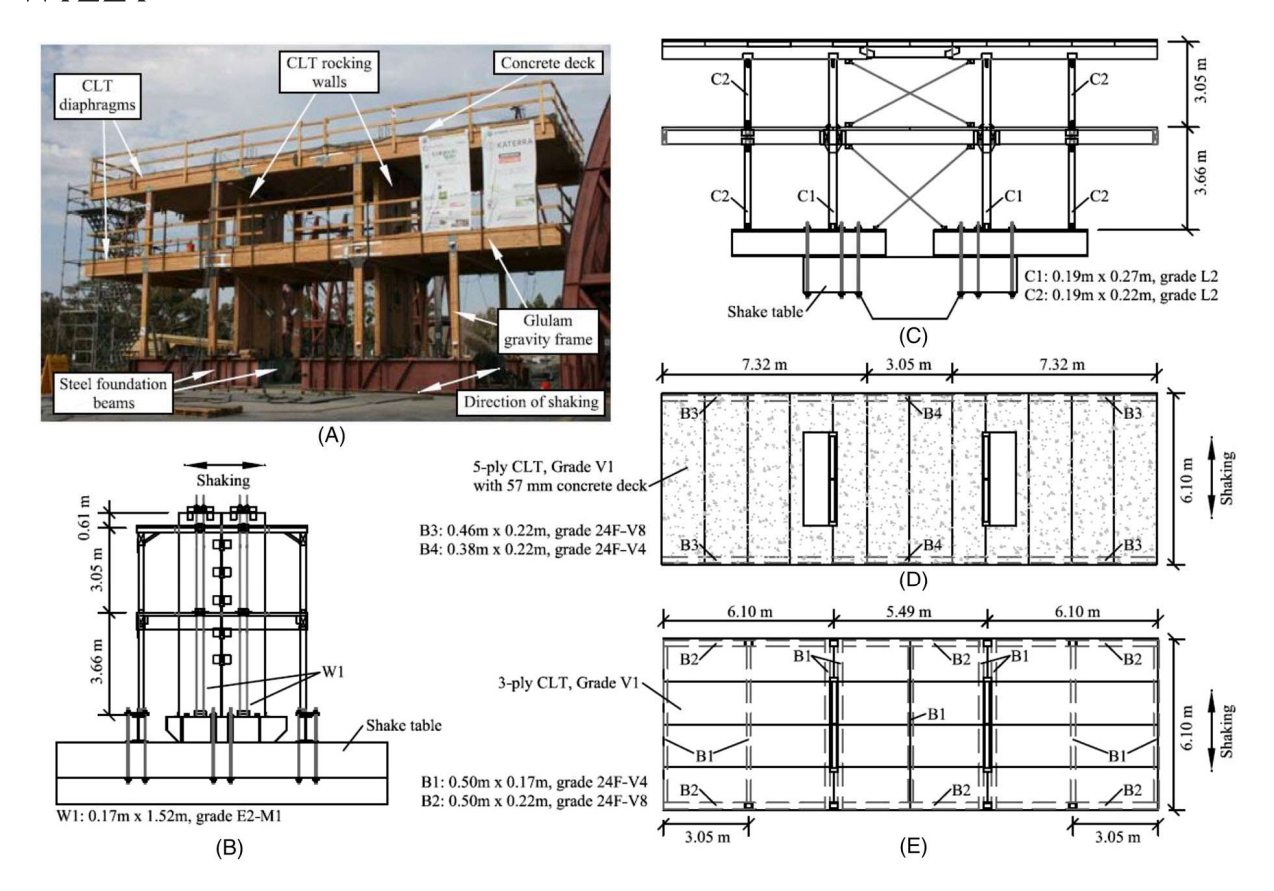


FIGURE 5 Two-story test building: (A) photo, (B) CLT rocking wall elevation view, (C) building elevation view, (D) roof plan view, and (E) floor plan view

3.2 | Gravity framing and diaphragm

The gravity frame, designed in accordance with the US 2015 National Design Specification for Wood Construction, ¹² consisted of glulam beams and eight glulam columns. The four inner columns (columns C1 in Figure 5C) were continuous through the diaphragm, demonstrating balloon framing. The outer columns (columns C2 in Figure 5C) were separated by the floor diaphragm, demonstrating platform framing. The connections between the beams and columns and at column bases utilized vertically slotted details to allow free rotation and minimize damage to columns, beams, and joints under large lateral drifts.

Also shown in Figure 5, the more flexible first-floor diaphragm was 3-ply CLT, while the roof diaphragm was 5-ply CLT with a 57 mm concrete composite deck. The spans between the beams supporting the diaphragm were designed to satisfy deflection and vibration requirements for the design office occupancy. The floor and roof diaphragms were designed to be damage-free under the planned seismic excitations and the differing stiffness of each level was intentionally a study parameter as discussed in Barbosa et al.⁷ Figure 5D and E show the plan views for the roof and floor diaphragms and show the orientations of the beams and CLT diaphragm panels tested on each level.

3.3 | Post-tensioned rocking CLT walls

The seismic force resisting system was designed to meet the seismic demands computed per ASCE 7–10¹³ for a class B soil site in San Francisco, California. A seismic force reduction factor (R) of 6, an importance factor of 1.0, and an approximate period per ASCE 7–10 were used to compute equivalent lateral force demands used in the design. The design spectral response acceleration parameter at short periods (S_{DS}) and at a period of 1 second (S_{D1}) were 1.06 and 0.34 g, respectively, and the approximate fundamental period (T_a) was 0.20 s.

TABLE 1 CLT wall panel dimensions and assumed material properties for design and modeling

b_w (m)	L_{w} (m)	h_{w} (m)	E_w (MPa)	G_w (MPa)	$f_{y,clt}$ (MPa)	$\varepsilon_{s,clt}$ (m/m)	$\varepsilon_{cr,clt}$ (m/m)
0.17	1.52	7.32	8536	552	25	0.0056	0.0375

The walls were designed such that the ELL moment, M_{ell} , could resist the design moment corresponding to seismic demands. M_{ell} was calculated using Equation (2), assuming a compression contact length, c, equal to $3L_w/8$ with a linear stress distribution in the CLT, initial PT bar forces, and fully yielded UFPs.

The full moment-rotation behavior of the coupled wall was also approximated to check a series of performance objectives. This behavior was approximated using the cross-section analysis procedure and the monolithic beam analogy, initially developed by Pampanin et al.¹⁴ for precast concrete frames and adapted by Newcombe et al.¹⁵ and Ganey⁴ for mass timber. The performance objectives used for the design of this test specimen were based on the performance objectives developed by Ganey⁴ with some modifications. They were as follows:

- 1. Immediate Occupancy: no required repair of the system after a service level earthquake (SLE), defined as earthquake intensity with 50% probability of exceedance in 30 years (43-year return period). Limited UFP yielding is allowed, however, PT bars and CLT walls should remain elastic. System reaches peak drifts of around 1%.
- 2. Limited Repair: allows significant yielding of the UFPs with potential replacement and full system recentering after a design based earthquake (DBE), defined as earthquake intensity with 10% probability of exceedance in 50 years (475-year return-period). While UFPs can be heavily damaged and thus replaced, PT bars should not yield and CLT panels should see minimal damage. Story drifts should be limited to 2%.
- 3. Collapse Prevention: limited overall damage to the system to prevent collapse after a maximum considered earthquake intensity (MCE_R), defined here as the MCE_R earthquake intensity from ASCE 7–10. PT bars can experience minor yielding and wall corners can reach strains that indicate localized crushing, but damage should be limited to prevent any major loss of strength or stiffness. Story drifts should be limited to 4%.

The four CLT wall panels were 5-ply, grade E2-M1 CLT. Each panel was balloon framed, such that the top of the walls extended 0.61 m above the roof. The material properties and compression behavior used for the CLT panels in design were approximated as shown in Figure 3, based on test results from previous CLT testing. Table 1 summarizes the wall dimensions and the assumed CLT compression properties based on the test results.

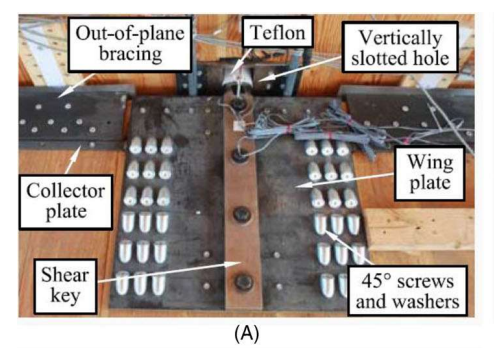
Each wall panel was post-tensioned with four bars that spanned the entire height of the wall. The bars were Simpson Strong-Tie, ATS high-strength, fully threaded, 19-mm diameter rods (with a net tensile area, $A_{net,pt}$, of 215 mm² and an elastic modulus, E_{pt} , of 2×10⁵ MPa). The listed yield and ultimate stresses were 634 and 827 MPa, respectively. As shown in Figure 6B, PT bars were anchored to the top of each CLT wall panel with a fabricated steel saddle. While recording the applied force using load cells, each bar was manually tightened to an initial force, $T_{0,pt}$, of 53 kN, about 40% of the yield force. At the base of the wall, a steel post-tensioning hold down plate was welded to the steel foundation beam anchoring the PT bars to the foundation, as seen in Figure 6C.

Also seen in Figure 6C, shear transfer angles were welded to the foundation beam at either end of the wall to transfer shear forces from the wall panels to the foundation beam. To prevent out-of-plane movement at the wall bases, a series of out-of-plane restraint angles were also welded to the foundation beam, against the faces of the walls.

The UFP energy dissipaters were designed to provide a minimum energy dissipation ratio, β , of 0.3 per the recommendations of Christopoulous et al. ¹⁶ The ratio, β , is approximated as the ratio of the idealized flag-shape damping hysteresis area to the area of the idealized full elastic-plastic hysteresis, calculated as:

$$\beta = \frac{M_{ufp}}{2M_y} = \frac{n_{ufp} \left(V_{ufp} L_w \right)}{2 \left[n_p \left(T_{o,pt} + W \right) d \right]} \tag{3}$$

where M_{ufp} , is the moment due to the UFPs in the system and M_y is the idealized yield moment in the system.¹⁷ For this design, M_y was taken as the ELL moment, M_{ell} , ignoring the contribution of the UFPs. Figure 6D shows one of the UFPs used to couple two CLT panels to form each wall. After initial post-tensioning of the walls, bolts were used to attach the UPFs to steel saddles that were anchored to the wall panels. The UFP properties, including dimensions and the elastic modulus, E_{ufp} , and yield stress, $f_{v,ufp}$, of the steel used are summarized in Table 2.



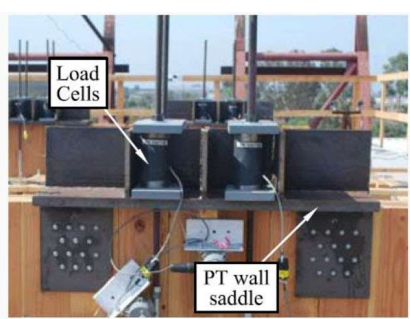
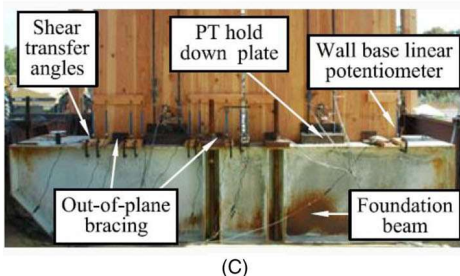


FIGURE 6 CLT rocking wall connection details: (A) wall-to-diaphragm shear transfer connection and out-of-plane bracing; (B) top of wall PT wall saddle connection; (C) base of wall shear transfer, bracing, and PT hold down connection; and (D) UFP energy dissipater connection



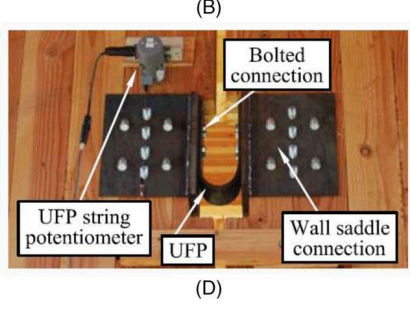


TABLE 2 UFP dimension and material properties

\boldsymbol{b}_{u} (mm)	t_u (mm)	D_u (mm)	E_{ufp} (MPa)	$f_{y,ufp}$ (MPa)
114	9.5	92.1	2×10 ⁵	414

TABLE 3 Dimensions and properties of diaphragm-to-wall shear key transfer connection

Level	w_{key} (mm)	t_{key} (mm)	L_{key} (mm)	E_{key} (MPa)
Roof	67.5	44.5	416	2×10 ⁵
Floor	73.0	22.2	416	2×10 ⁵

The rocking wall lateral system connected to the diaphragm using the vertically slotted shear key connection detail shown in Figure 6A. Originally, developed for the Framework project in Portland, OR, ¹⁸ the connection transferred shear forces between the diaphragm and the rocking shear walls while keeping the diaphragm level by allowing uplift of the wall panels relative to the diaphragm. As seen in Figure 6A, a rounded cantilevered steel shear key (width, w_{key} and thickness, t_{key}) was inserted into a vertically slotted hole to create a slotted pin connection allowing vertical and rotational movement to decouple the diaphragm from the rocking walls. To reduce resistance at the interface in the vertical direction, the shear key was wrapped in a thin Teflon sheet. One end of the shear key was bolted to a steel wing plate to transfer load from the shear key to the diaphragm. The shear key cantilevered a length, L_{key} , measured from the centroid of the wall to the edge of the wing plate. A 45-degree timber screws and washers anchored the wing plate to the CLT diaphragm. Also seen in Figure 6A, collector plates, welded to the wing plate, ran along the width of the diaphragm (parallel to the wall faces). Timber screws anchored the collector plates to the diaphragm. The connection was designed based on the estimated rocking wall capacity at 4% drift with an additional safety factor of 1.5. Table 3 summarizes the properties of the shear keys used on the roof and floor level. In addition, adjacent to the shear-transfer connection, a series of angles provided out-of-plane bracing as shown in Figure 6A.

4 | TESTING PROGRAM

Prior to testing, a white noise excitation was run to obtain the approximate first mode elastic period of 0.9 s. 5,24 Four ground motion records from the NGA West PEER ground motion database 19 were then scaled to represent the three hazard levels (SLE, DBE, and MCE_R) used to establish the performance objectives described previously. For each hazard level, the ground motion records were scaled such that the average of the spectra did not fall below the uniform hazard spectra or response spectra at 0.9 s, the approximate first mode fundamental period.

TABLE 4 Ground motion testing sequence

	PEER-NGA Groun Information							
Test	Event Name	Station Name	RSN- Component	Hazard Level	Target SF	Effective SF	Effective PGA (g)	Effective Sa @ 0.9 sec (g)
1	Loma Prieta	Capitola	752-2	SLE	0.42	0.36	0.16	0.15
2	Loma Prieta	Capitola	752-2	SLE	0.44	0.38	0.18	0.16
3	Northridge	Canoga Park	959-2	SLE	0.28	0.25	0.19	0.18
4	Superstition Hills	Poe Road	725-2	SLE	0.40	0.37	0.13	0.12
5	Northridge	Canoga Park	959-2	DBE	1.00	0.99	0.53	0.69
6	Northridge	Canoga Park	959-2	DBE+	1.06	1.13	0.52	0.74
7	Imperial Valley	Delta	169-1	SLE	0.50	0.42	0.13	0.21
8	Northridge	Canoga Park	959-2	DBE+	1.06	1.13	0.53	0.74
9	Loma Prieta	Capitola	752-2	DBE	1.21	1.16	0.52	0.49
10	Superstition Hills	Poe Road	725-2	DBE	1.42	1.41	0.44	0.42
11	Loma Prieta	Capitola	752-2	MCE_R	1.37	1.32	0.62	0.57
12	Northridge	Canoga Park	959-2	MCE_R	1.32	1.31	0.73	0.91
13	Superstition Hills	Poe Road	725-2	MCE_R	1.98	2.06	0.63	0.63
14	Northridge	Canoga Park	959-2	$MCE_R \times 1.2$	1.60	1.57	0.85	1.11

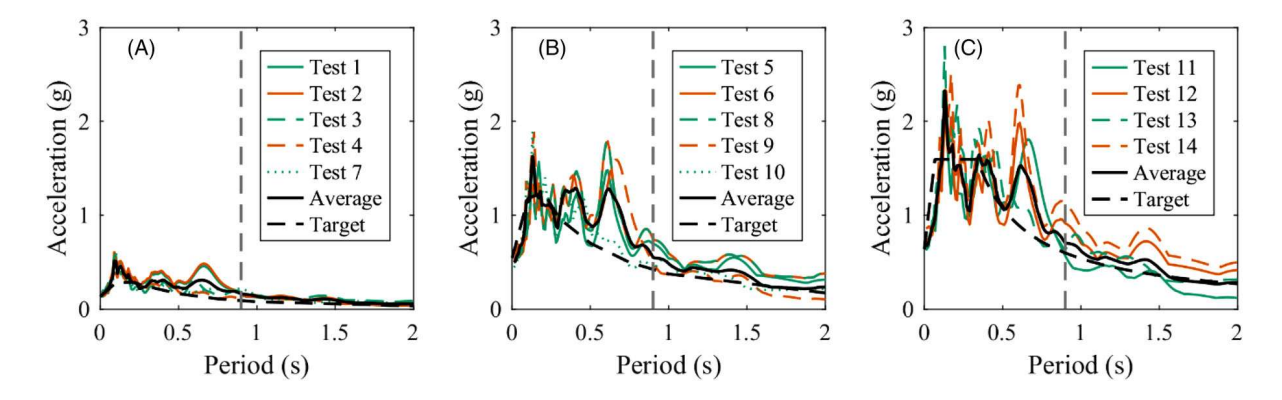


FIGURE 7 Effective spectral acceleration spectra of (A) SLE, (B) DBE, and (C) MCE_R level ground motions

Summarized in Table 4, the specimen was subjected to fourteen ground motion records, selected from the group of scaled motions. The target scale factor is the intended scale factor for the ground motion file, while the effective scale factor is the average ratio of the output response spectra to the unscaled input response spectra between the periods of 0.4 and 2 s. The difference in these two factors results from inherent error in the shake table. The effective peak ground acceleration (PGA) and the spectral acceleration at a period of 0.9 s are taken from the output ground motion files. Note that tests 6 and 8 used the Northridge motion scaled to be slightly larger than DBE and was repeated back-to-back to demonstrate the ability of the building to withstand multiple strong motions without the need for repair between motions. The PT bars did not yield during any MCE_R level motions, so the Northridge MCE_R level motion was scaled by a factor of 1.2 for test 14 to study the response of the building with yielded PT bars.

Figure 7A and B show the target uniform hazard spectra for the SLE and DBE hazard levels respectively, and Figure 7C shows the MCE_R response spectra. Each figure also includes the response spectra for the effective ground motions and their average response spectra. In Figure 7B, tests 6 and 8 are not included in the calculation of the average DBE hazard level because they are slightly larger than DBE. Similarly, test 14 was not included in the calculation of the average spectrum for motions scale to the MCE_R hazard level because it was scaled to be 1.2 times the MCE_R spectrum at the building's period. As shown, the average spectral acceleration of each ground motion set at the building's approximate period (0.9 s) exceeds the target hazard level spectral accelerations. This is because the effective ground motions recorded from the

FIGURE 8 Wall base and foundation beam, (A) photo of gap at base of the wall panel and the foundation beam at the end of testing, (B) yielded foundation beam schematic elevation view, and (C) cross-section view

shake table were slightly larger than the input motions and because the smallest ground motion in the scaled set was not run.

4.1 | Experimental observations

The overall response of the structure was symmetric, both coupled walls performed almost identically, and displacements across the diaphragm indicated little torsion, as intended in the design. In general, minimal damage to the structure was observed and the walls met all design performance objectives with respect to drift, PT bar yielding, UFP yielding, and damage to the CLT at the base of the wall. 5,24 The walls performed better than expected, with no PT bar yielding observed until larger than MCE_R level ground motions were run. There was no major structural damage or crushing at the rocking corners of the walls during any of the tests.

Figure 8A shows an image of one wall panel corner; a gap is notable between the wall toe and the foundation beam. After removing the walls at the end of testing, it was determined that this gap was a result of both foundation beam deformation and CLT deformation, with the former contributing more substantially. Figure 8B shows an exaggerated elevation view schematic of the yielded foundation beam and Figure 8C shows the corresponding section view of the foundation beam. The permanent vertical deformation at the corners of the panels, d_f , ranged from 6.9 to 12.2 mm, and the length over which this deformation occurred, l_f , ranged from 203 to 356 mm. Welding the thick PT anchorage plates to the foundation beam at the centerline of each wall panel effectively stiffened the foundation beam in these locations. As a result, this portion of the foundation beam saw no permanent deformations and elastic deformations were not observed in video footage. It is assumed that these portions of the foundation beam remained essentially rigid while the corners were flexible as shown in Figure 8B.

Although the permanent deformation after every test was not measured, the gaps observed in Figure 8A appeared early on during the testing sequence and gradually increased in size throughout testing. The flexibility of the foundation beams is believed to have altered the behavior of the specimen from the designed case with a rigid foundation. The foundation flexibility observed is unique to this test and a more rigid foundation would be expected in actual buildings.

5 | NUMERICAL MODEL

Two numerical models were developed using *OpenSees*²⁰ and built upon techniques presented in Ganey.⁴ While the techniques presented in Ganey⁴ have been previously validated using cyclic loading test results, this study aims to also validate them for nonlinear dynamic time history analyses. The first model included the flexibility of the foundation beam and is intended to replicate the test results and verify the modeling techniques. The second model replaces flexible foundation beam with a rigid foundation boundary condition and is intended to predict the response of the specimen had it been tested with a more rigid foundation. Both models were two dimensional, representing one of the coupled walls in the test specimen, with half the gravity system included and half the mass. Figure 9 shows a schematic of the numerical model including foundation flexibility and conceptual behaviors of various component models used within the model.

The PT bars were modeled using corotatinal truss elements that connected to a fixed node at the base and to the end of a cantilevered rigid element at the top of the wall representing the PT offset from the centerline of the wall. A bilinear

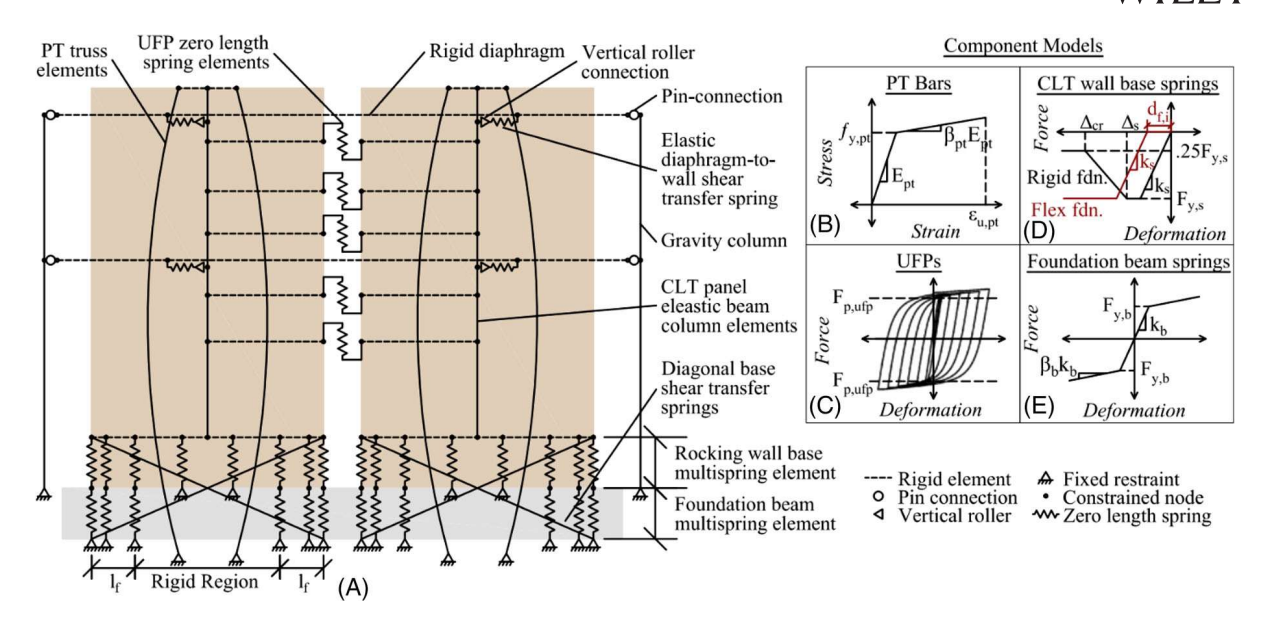


FIGURE 9 Numerical model schematic and material models used to model the two-story specimen

hysteretic material model with damage (Elastic PPGap material in OpenSees) limited the element behavior to tension only and allowed for damage accumulation after yielding (shown in Figure 9B). An initial strain wrapper (InitStrainMaterial in OpenSees) was applied to simulate prestressing in the elements. To correct for elastic wall shortening with application of the initial PT stress, a higher initial PT force $(T_{o,pt}^*)$ is applied in the model to ensure the target PT force $(T_{o,pt})$ is achieved. The larger applied PT force is calculated as:

$$T_{o,pt}^* = T_{o,pt} \left(\frac{k_w}{k_w - k_{pt}} \right) \tag{4}$$

where k_w is the elastic stiffness of the wall calculated as $A_w E_w/h_w$ and k_{pt} is the elastic stiffness of the PT bars calculated as $A_{nt} E_{pt}/h_w$.

Each UFP was modeled using a vertically orientated zero-length spring with a uniaxial Giuffrè-Menegotto-Pinto steel material model with isotropic strain hardening (Steel02 in *OpenSees*) as shown in Figure 9C. A yield force of 23.3 kN and a stiffness of 4.8 kN/mm were used, calculated using equations from Kelly et al.²¹ and Baird et al.,⁹ with properties from Table 2. The UFPs were located at the midpoint between the two wall panels and rigid elements connected each end of the UFP spring to each of the wall element at the same vertical position.

A series of elastic beam-column frame elements (ElasticTimoshenkoBeam element in *OpenSees*) that included axial, flexure, and shear deformations modeled the elastic portion of the CLT rocking walls. The CLT properties from Table 1 were used for these elements.

The inelastic compressive deformation of the CLT and the rocking behavior at the base of the panels was modeled using a multispring contact element, initially developed by Spieth et al. 22 for prestressed concrete structures. The wall base multispring element consisted of 40 parallel zero-length springs distributed along the length of the wall using a Labatto Integration method. The top of each spring connected to the base of the wall beam-column element with a horizontal rigid element. For the rigid foundation model, the bottom of each spring was fixed. For the flexible foundation model, the bottom of each spring within a distance of l_f from the corners of each wall panel was connected to an additional zero length spring modeling the foundation beam flexibility. The base of the remaining springs near the centers of each wall panel were fixed, modeling the portion of the foundation that was assumed to be rigid. Additionally, two stiff shear transfer springs were attached diagonally to the outer multispring and foundation beam springs to transfer shear without significantly inhibiting rocking action.

Each zero-length spring at the wall base is assigned the compression-only hysteretic material model shown in Figure 9D. The compression-only portion of the material model simulated the rocking behavior while the hysteretic properties simulated the CLT compression behavior. To transform the CLT stress-strain compression behavior shown in Figure 3 to a force-deformation behavior needed for zero-length springs (Figure 9D), a plastic hinge length, l_p , was chosen. In this



TABLE 5 Initial gap included in the model

Test numbers	$d_{f,i}$ (mm)
1-2	0.0
3–5	1.3
6–11	2.5
12–14	5.1

model, a plastic hinge length of $2b_w$ was assumed in accordance with Akbas et al.⁸ An overall contact stiffness, K_s , was determined for the entire wall base (all multispring elements representing the CLT) as:

$$K_{s} = \frac{A_{w}E_{w}}{l_{p}} \tag{5}$$

where A_w is the cross-sectional area of the wall panel equal to the product of b_w and L_w . Wall dimensions and material properties can be referenced in Table 1. Referring to Figure 9D, each individual spring stiffness, k_s , was a weighted portion of the overall contact stiffness, K_s , based on the Labatto Integration method. The product of the CLT panel yield stress and the Labbatto weighted area of each spring determined the yield strength of each spring, $F_{y,s}$. Similarly, the product of the respective strains, ϵ_s and ϵ_{cr} , and the plastic hinge length, l_p , determined the splitting deformation, Δ_s , and the crushing deformation, Δ_{cr} .

The addition of the wall base multispring elements increases the axial flexibility of the wall. Although small and unlikely to affect the performance dramatically, a simple truss element, spanning the length of the CLT beam-column wall elements, can be added to increase the area of the wall and compensate for the reduced stiffness. The truss element has an elastic material model, with elastic modulus E_w and an area, A_w^* calculated as:

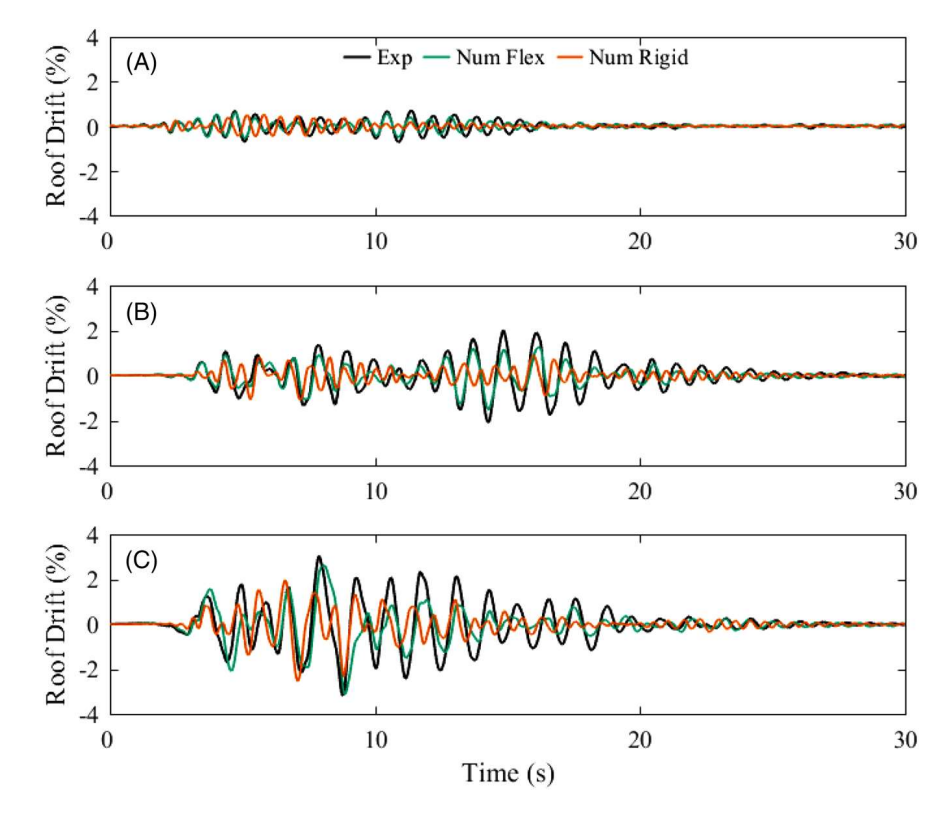
$$A_w^* = \frac{l_p}{h_w - l_p} \tag{6}$$

In the flexible foundation model, the foundation beam was assumed to be undamaged at the beginning of the first two ground motions. Subsequently, an initial permanent deformation of the foundation beam was assumed at the beginning of the tests from accumulated foundation beam damage. Thus, a compression gap was introduced to the CLT wall base springs in the model. The size of the gap decreased linearly along the flexible foundation portions of the beam with the corner springs having an initial gap length of $d_{f,i}$ and the springs located at a distance of l_f from the corners having no initial gap. A flexible foundation length (l_f) of 0.61 m was used for all tests. The gap values $(d_{f,i})$ used for each test are shown in Table 5 and are based on observations made during the testing. As shown in Figure 9D, for the flexible foundation model, a compression only elastic-perfectly plastic material with a gap (ElasticPPGap in *OpenSees*) was used to achieve the initial stiffness of the CLT and account for the initial gap. Although this material model cannot capture the deterioration, the CLT remained elastic, so it did not affect the behavior.

A multilinear material model (Steel01 in *OpenSees*) modeled the foundation beam flexibility, as shown in Figure 9E. The approximated stiffness of the foundation beam springs was calculated assuming the top flange of the double webbed beam shown in Figure 8C acted as a fixed-fixed beam between the two webs and the base of the wall imposed a uniformly distributed load (along a length equal to the panel thickness, b_w) at the center of the beam. The thickness of the top flange (t_f) was 15.9 mm and the webs were spaced at a distance (d_f) of 138 mm. The elastic stiffness of the beam was calculated for the flange dimensions and loading, and the yield force was approximated using plastic analysis. The stiffness (k_b) and yield force $(F_{y,b})$ of each spring was calculated as a weighted portion of the total stiffness and yield force using the same Labatto Integration distribution as the rocking wall base multispring element. A yield stress of 414 MPa was assumed for the steel beam. Note, the methods used to justify the flexible foundation beam material are custom for this test, however, the multispring approach could be used for other forms of flexible foundations.

The gravity columns were modeled with two continuous elastic beam column elements with cross-sectional areas representative of the continuous and platform columns and moment of inertias corresponding to only the continuous, balloon framed columns. Equivalent gravity loads and seismic masses were applied to each gravity column at each floor level. Rigid elements connected the gravity columns to the wall panels at each floor level simulating a rigid diaphragm. As discussed by Hasani et al., ²³ the rigid diaphragm model assumption can predict the fundamental mode behavior and peak

FIGURE 10 Comparison of the roof drift time history response from experimental results, the flexible foundation numerical model, and the rigid foundation numerical model for (A) Test 1, SLE Loma Prieta, (B) Test 10, DBE Superstition Hills, and (C) Test 12, MCE_R Northridge



story drifts well, but the flexibility in the diaphragm should be included to predict the higher frequency motion and floor accelerations.

The connection between the diaphragm and walls was modeled with a zero-length spring. To model the elastic flexibility of the wall-to-diaphragm connection, the material properties assigned to the horizontal degree of freedom of the zero-length spring were that of a cantilever beam with the dimensions of the shear key listed in Table 3. The spring had zero stiffness in the vertical and rotational degrees of freedom to allow for uplift and rocking.

6 | DISCUSSION OF EXPERIMENTAL AND ANALYTICAL RESULTS

The following section presents results from the flexible foundation model and rigid foundation model with the experimental results. The flexible foundation model is intended to match the experimental results and verify the modeling techniques as it more correctly models experimental boundary conditions. The intention of also presenting the results of the rigid foundation model is not to match the experimental results, but to predict how the specimen would have behaved with the as designed rigid foundation boundary condition. First, a discussion comparing the experimental results to the numerical model including foundation flexibility will be presented. Then, the experimental results will be compared to the rigid foundation model to study how the structure's behavior would have changed had it been tested with a rigid foundation boundary condition. Finally, the results from the rigid foundation model were assessed to determine if the structure would have met all design performance objectives.

6.1 Comparison of numerical model including foundation flexibility with experimental results

Experimental drift results were determined by averaging and double integrating recordings from seven accelerometers located on each diaphragm level. As discussed in Pei et al.,⁵ first-mode response dominated such that all interstory drifts were similar. The numerical model showed similar results, thus only the roof drifts are presented and discussed. Figure 10 compares the time history roof drift response from the experimental results with the flexible foundation numerical model for three of the tests, each at a different intensity level. As shown, the numerical model very accurately replicated the period

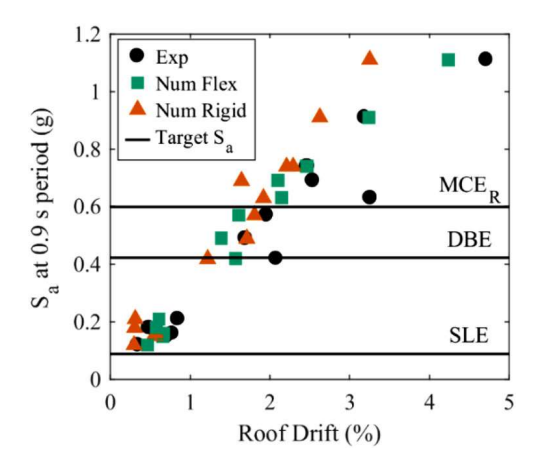


FIGURE 11 Comparison of peak roof drift values from the experimental results, the flexible foundation numerical model, and the rigid foundation numerical model

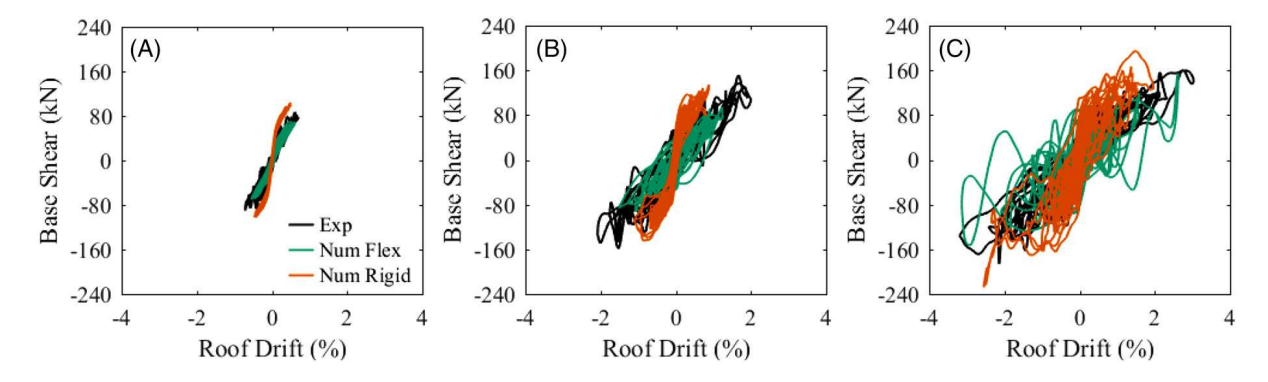


FIGURE 12 Comparison of the hysteretic response from experimental results, the flexible foundation numerical model, and the rigid foundation numerical model for (A) Test 1, SLE Loma Prieta, (B) Test 10, DBE Superstition Hills, and (C) Test 12, MCE_R Northridge

and overall behavior, but under predicted the peak drift values. The maximum absolute roof drift for the experimental and numerical results for all 14 tests are summarized in Figure 11 which plots the spectral acceleration of each ground motion at the approximate period of the building (0.9 s) versus the peak roof drift value. The figure shows a clear positive trend between the increasing spectral acceleration and increasing drift ratios. It also shows that the numerical model with foundation flexibility underestimates the peak drifts.

Assuming a rigid diaphragm, experimental base shear results were approximated by calculating the inertial force at each floor by multiplying the average of the accelerometer readings on each story by the estimated mass on each story. Figure 12 shows the base shear versus roof drift hysteretic response for the experimental and numerical results for the same three tests shown in Figure 11. Relatively good agreement of the overall structure stiffness is shown, but the base shear values are slightly underestimated with the numerical model. Again, Figure 13 summarizes the peak base shear values obtained from each test plotted against the spectral acceleration from the recorded table motion at the building's measured first natural period. Here, the experimental values are consistently larger than the numerical results. Note that results for a single coupled wall are shown in Figures 12 and 13.

The PT bar forces were measured using load cells. Figure 14 shows the PT bar force normalized by the bar yield force (taken as the manufactures specified yield stress times the tensile area) versus roof drift for an SLE, DBE, and MCE_R level ground motion. For each test, the figure shows the four PT bar locations along the face of the coupled wall, as denoted by the graphics on each plot. A plot of the peak PT force for each test versus the ground motions spectral acceleration at the building's period is plotted in Figure 15. As seen in Figure 14, the general behavior of the PT bars is well predicted by the numerical model, but also underestimates peak PT force values. The underestimated peak PT force values with the numerical model is expected because the roof drift values are also underestimated, meaning the walls do not lift as much and the PT bars elongate less than in the tests. Further, the flexibility of the foundation beam resulted in downward sinking movement of the walls when rocking, decreasing bar elongation.

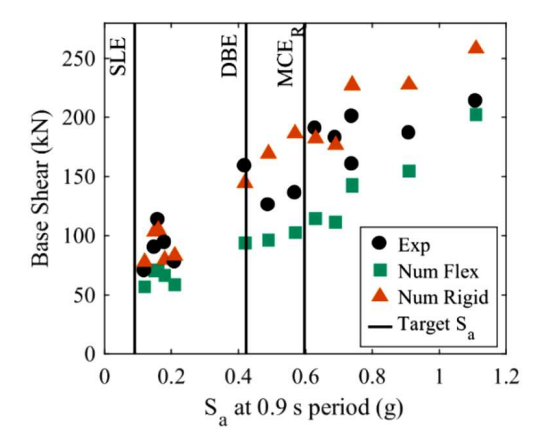


FIGURE 13 Comparison of peak base shear values for a single wall from the experimental results, the flexible foundation numerical model, and the rigid foundation numerical model

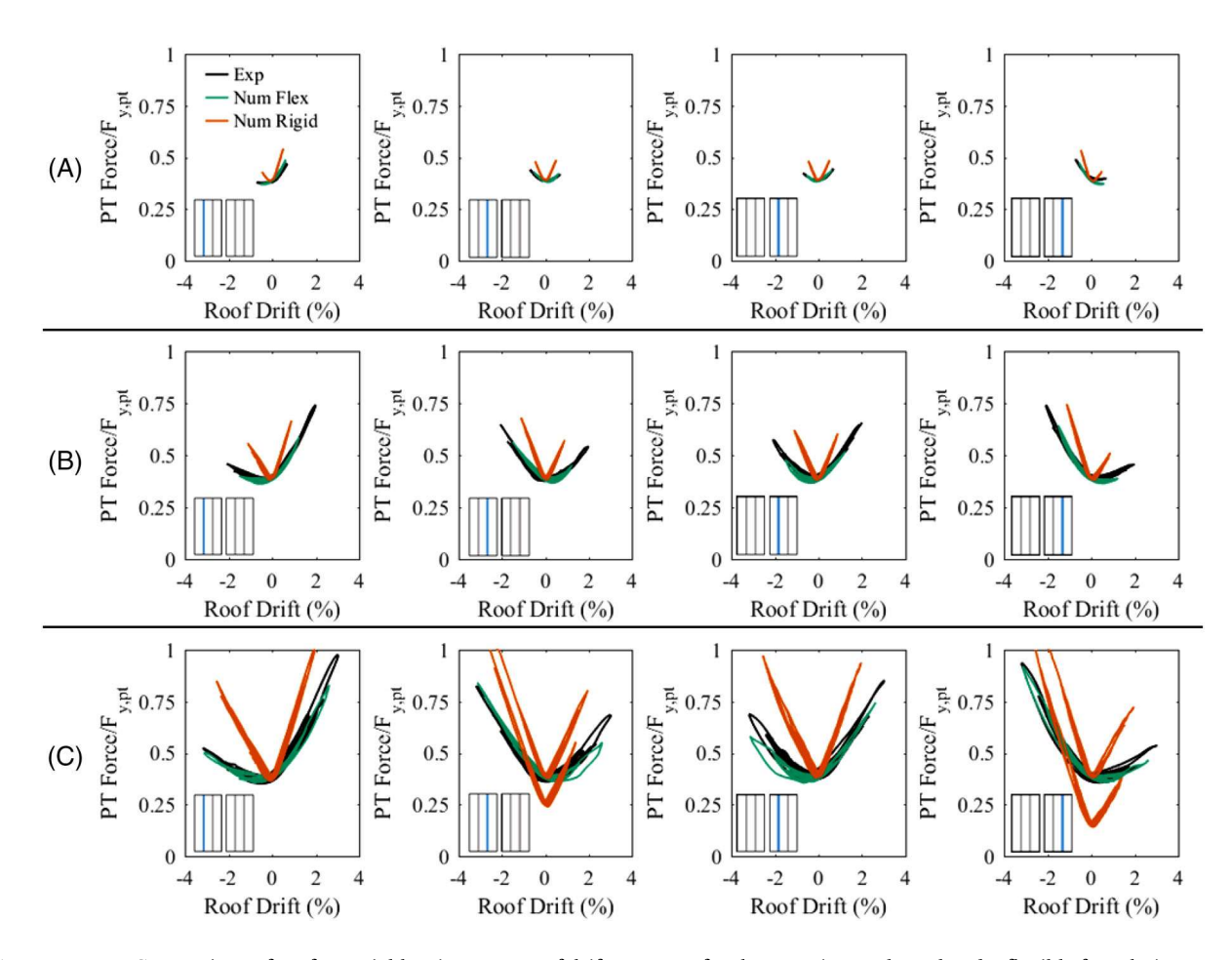


FIGURE 14 Comparison of PT force yield ratio versus roof drift response for the experimental results, the flexible foundation numerical model, and the rigid foundation numerical model for (A) Test 1, SLE Loma Prieta, (B) Test 10, DBE Superstition Hills, and (C) Test 12, MCE_R Northridge

String potentiometers measured UFP deformation, as shown in Figure 6D. A ratio of peak to yield displacement was used to quantify a measure of UFP ductility demand. Figure 16 shows the spectral acceleration at the building's period versus peak UFP yield displacement ratio for all tests. As shown in the figure, the UFPs yielded in almost every test and the energy dissipation increased with increasing ground motion intensity, as expected. Because the numerical model with foundation flexibility under predicts roof drift, it also under predicts the UFP yield displacement ratio.

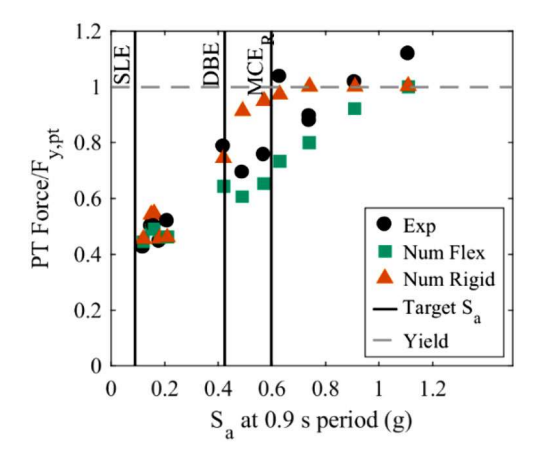


FIGURE 15 Comparison of peak PT force yield ratios from the experimental results, the flexible foundation numerical model, and the rigid foundation numerical model

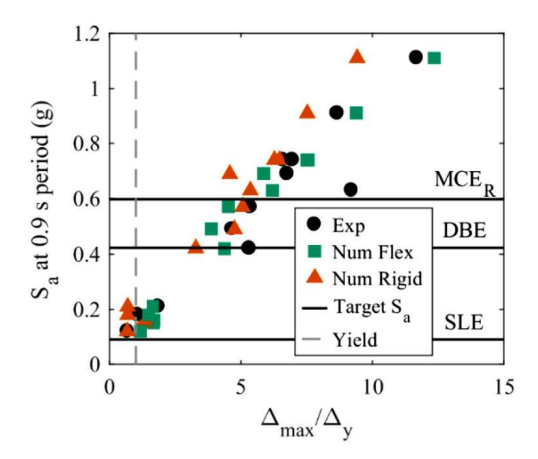


FIGURE 16 Comparison of peak UFP yield displacement ratios from the experimental results, the flexible foundation numerical model, and the rigid foundation numerical model

Linear potentiometers installed at the corners of the wall panels (Figure 6C) were used to investigate positive uplift rotations and negative compression rotations at the wall base. The vertically orientated potentiometers were anchored to the portion of the foundation beam flanges outside of the webs (the portion of the foundation beam that did not deform). The downward deformation recorded by these potentiometers was intended to measure compression deformations of CLT. However, because the deformations from foundation beam flange flexibility were substantially larger, the recorded deformations were assumed to be fully attributed to foundation beam deformations. The base rotation was approximated by dividing the recordings by the CLT wall panel length (L_w). Figure 17 plots a time history calculated from one of the potentiometers. Similarly, the numerical results are calculated by dividing the displacement recorded by the top node of the outermost spring in the wall base multispring element by the length of the CLT wall panel (L_w). Because the springs at the base of the numerical model are all zero-length, this recorded deformation includes the uplift and deformations of the CLT wall panel and foundation beam.

Because the numerical model underestimates the peak drift values it is logical that the rotations in Figure 17 are also underestimated, however, there is good agreement in the general shape of the response. While uplift rotations are underestimated by the model, the negative or compressive deformation are slightly overestimated, indicating that the material model used for the foundation beam flange behavior in the numerical model may have been too flexible. Figure 18 summarizes the peak uplift rotations and peak compressive rotations observed in each test. Again, this figure shows that the numerical model with foundation flexibility underestimates uplift rotations and overestimates compressive rotations. The overestimation of the compressive rotations could partially explain the underestimation of the uplift rotations (and similarly the drifts and PT forces) since the wall is settling into the foundation beam more instead

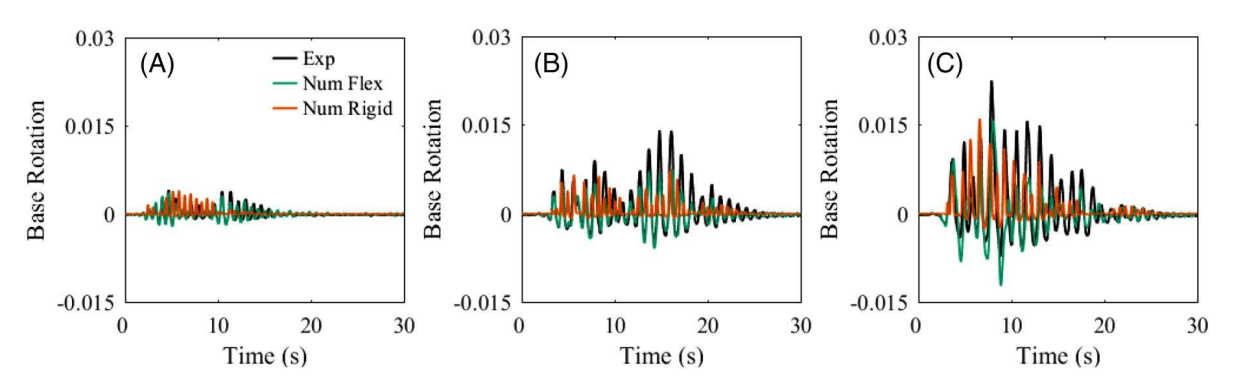


FIGURE 17 Comparison of CLT wall panel base rotation from experimental results, the flexible foundation numerical model, and the rigid foundation numerical model for (a) Test 1, SLE Loma Prieta, (b) Test 10, DBE Superstition Hills, and (c) Test 12, MCER Northridge

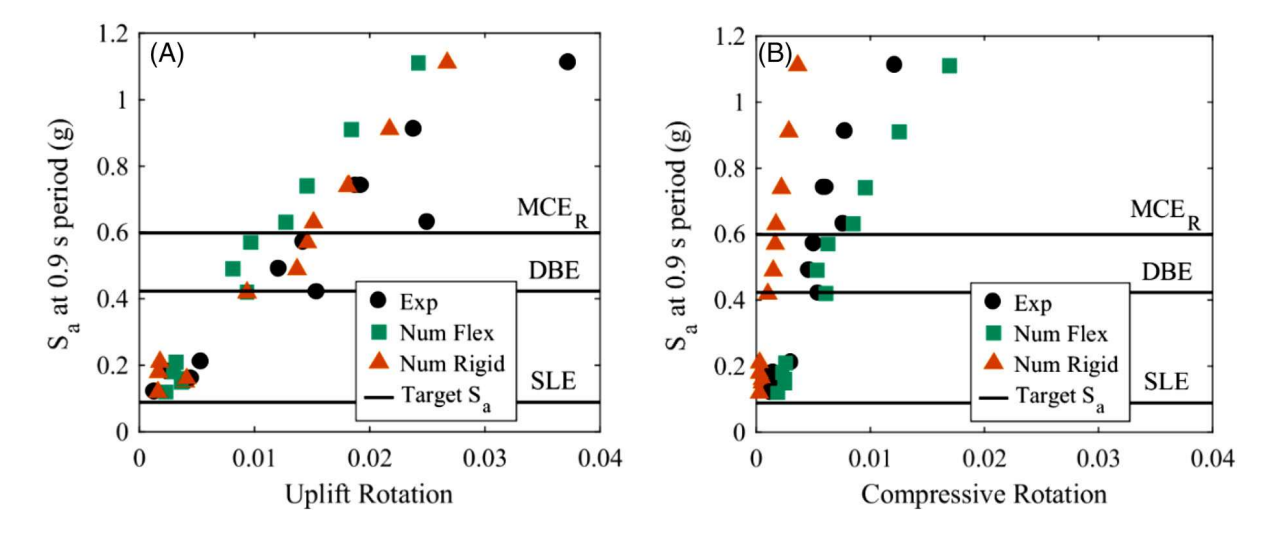


FIGURE 18 Comparison of peak wall base (a) uplift and (b) compressive rotations from the experimental results, the flexible foundation numerical model, and the rigid foundation numerical model

of lifting and rocking up. However, apart from peak values, the overestimation of the downward rotations appears to be smaller than the overestimation of the uplift rotations, thus only partially explaining the differences.

Due to the unforeseen flexibility in the foundation beam, instrumentation during testing did not accurately measure axial deformations in the CLT at the wall base. However, there was no visual damage to the base of the walls after demolition of the structure; the bases of the walls were largely square. Similarly, in the numerical model with foundation flexibility, the deformations of the wall base multispring element springs remained below the yield deformation (Δ_y) , calculated by dividing the yield force of each spring $(F_{v,s})$ by the stiffness of each spring (k_s) .

Overall, the presented numerical model including foundation flexibility does a good job of predicting the response of the tested structure and thus similar modeling techniques can be used to predict the response of structures with comparable rocking wall systems with confidence.

6.2 Comparison of numerical model without foundation flexibility with experimental results

Because the foundation flexibility was unexpected, it is important to quantify impact of the foundation flexibility on the overall behavior and to explore if the design would still meet performance objectives with the intended rigid foundation behavior. Thus, the rigid foundation numerical model was created as discussed above.

Figure 10 includes results from the numerical model with the rigid foundation. In comparison to the flexible foundation model that was intended to replicate test results, the change in foundation boundary condition does have a significant

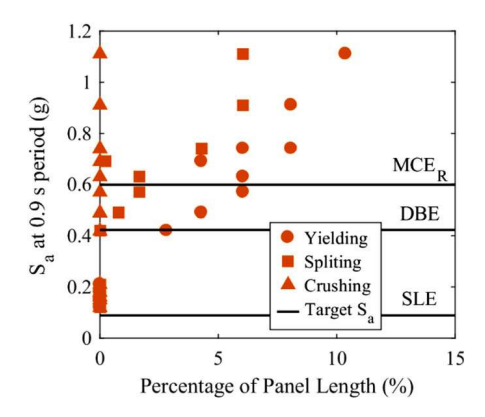


FIGURE 19 Rigid foundation numerical model results only; spectral acceleration at the building's period for all tests versus the percentage of the panel length exceeding the CLT damage state of yielding, splitting, and crushing

effect on the overall response. The period appears to be shorter with the rigid foundation as a result of the increased system stiffness. The increased stiffness also results in smaller roof drifts, as seen in Figure 11.

The impact of the increased stiffness with the rigid foundation model is also clearly shown in the hysteretic response shown in Figure 12. It is also interesting that the idealized flag shape response of rocking systems is more apparent in the response for the rigid foundation model. With a rigid foundation, major hysteretic damping does not occur until after the ELL when the wall begins to uplift, and the UFPs experience large deformations. However, with the flexible foundation beam, nonlinearity in the foundation occurs prior to the ELL, resulting in increased damping. This is clear from Figure 12A, an example of an SLE test. For the rigid foundation model, the response is bilinear, the peak response has just exceeded the ELL, and there is minimal damping. In comparison, for the flexible foundation model, while the response is more linear than the comparable DBE and MCE_R response (Figure 12B and C, respectively) there is an increase in damping from the foundation beam deformation. Additionally, the increased system stiffness in the rigid foundation model results in increased peak base shear values as shown in Figure 13.

Because the rigid foundation model has smaller drifts, a decrease in peak PT forces may be expected, however, the rigid foundation model resulted in increased peak PT bar forces as shown in Figure 15 because the point of uplift shifts toward the compression toe of the wall panels, resulting in more elongation of the PT bars for a given roof drift when compared to the flexible foundation model. In the flexible foundation model, as the walls rocked the base of the wall sunk into the beam, flattening the response such that PT bar forces remained constant at low drifts, despite increasing drifts, as shown in Figure 15.

With the rigid foundation model, the UFPs still yielded during smaller hazard level earthquakes, as shown in Figure 16. However, because the drifts were smaller for the rigid foundation model, the peak UFP deformations were also slightly smaller. This resulted in slightly less damping as a result of UFP behavior in the rigid foundation model.

The base rotation response histories shown in Figure 17 and the peak uplift rotations summarized in Figure 18A indicate that the rigid foundation model had slightly higher uplift rotations than the flexible foundation model. The decrease in drifts with the rigid foundation model would typically result in decreased uplift rotations, however, since the point of uplift of the wall shifted toward the compression toe of the wall panels in the rigid foundation model instead of sinking into the foundation beam uplift rotations increased. The summarized compression rotations in Figure 18B show a major decrease in compressive base rotations in the rigid foundation model. While the compressive rotations were almost entirely a result of foundation beam deformations in the flexible foundation model, the compression rotations in the rigid foundation model are solely the result of deformations in the CLT.

The CLT deformations observed in the rigid foundation model resulted in predicted damage to the CLT base. Because no CLT damage was observed in the experiments or in the numerical model with the flexible foundation, Figure 19 only summarizes CLT damage results for the rigid foundation model. Figure 19 plots the spectral acceleration at the building's approximate period versus the percentage of damaged panel length. For each damage state, the length of the panel base over which spring deformations exceed the respective deformation limit (Δ_y for yielding, Δ_s for splitting, and Δ_{cr} for crushing), was recorded. Of the four wall panel corners, Figure 19 summarizes the maximum length as a percentage of the total wall panel length (L_w). While the strongest motions experienced some CLT yielding and splitting, CLT crushing was not observed in the simulations of any of the tests with the rigid foundation model.

6.3 | Performance of the numerical model without foundation flexibility with respect to design criteria

The CLT rocking wall system met all design performance objectives during testing. 24 However, it is clear that the flexibility in the foundation beams altered the performance of the specimen. Because the specimen was designed to rock on a rigid foundation and because realistic buildings would have rigid foundations, it is important to assess if performance objectives would have still been met had it been tested with a rigid foundation. The building was designed to meet three performance objectives: (1) immediate occupancy after SLE earthquakes, (2) limited repair after DBE earthquakes, and (3) collapse prevention after MCE_R earthquakes. To meet each of these three performance objectives, target drifts and damage criteria had to be met for the UFPs, the PT bars, and the CLT at the wall base.

Because many of the motions exceeded the target spectral acceleration of the intended hazard level at the building's period of 0.9 s, performance objectives were assessed by looking at the general trends instead of performance at each individual ground motion. For example, ground motions 6 and 8 were scaled to be DBE level earthquakes; however, with a spectral acceleration of 0.74 g at the building's 0.9 s period, they are most likely more representative of an MCE_R ground motion which has a target spectral acceleration of 0.60 g at 0.9 s.

To meet the drift criteria of the performance objectives, SLE, DBE, and MCE_R level earthquake should remain under 1%, 2%, and 4%, respectively. As seen in Figure 11, the drifts for the numerical model with the rigid foundation satisfy these criteria for all ground motions. Interestingly, the largest ground motion (that had a spectral acceleration 85% larger than the target MCE_R ground motion) only had a peak roof drift of 3.2%, using the rigid foundation model.

The design performance objectives allow for initial UFP yielding under SLE earthquakes and the UFPs can undergo large deformations beyond yield during DBE and MCE_R level earthquakes. The intent is to replace the damaged UFPs after DBE and MCE_R level earthquakes but should not need replacement after SLE level earthquakes. The peak UFP yield displacement ratios summarized in Figure 16 show that UFP criteria is met for all ground motions for the rigid foundation numerical model. Only one earthquake within the SLE region caused UFP yielding.

With target performance objectives, the PT bars were designed to remain elastic during SLE and DBE earthquakes and were allowed to yield during MCE_R earthquakes. The rigid foundation numerical results in Figure 15 show that PT bar yield criteria was met for all performance objectives. Note that while both the rigid foundation numerical model results and the experimental results met PT bar performance objectives, the rigid foundation results are closer to the limits of these performance objectives, but also are much closer to the intended design performance.

Finally, to meet performance objectives, the CLT at the base of the wall has to remain elastic during SLE earthquakes, should only have some damage during DBE earthquakes, and can have repairable damage under MCE_R level earthquakes. For the rigid foundation numerical model, Figure 19 shows that ground motions at the SLE hazard level resulted in no CLT yielding, ground motions at the DBE hazard level resulted in some yielding and a small amount of splitting, and the ground motions in the MCE_R region saw significant yielding and minor splitting. However, no CLT crushing was observed in any of the ground motions in the simulations with the rigid foundation model. These would all be considered to meet performance objectives. Again, note that while performance objectives are met for both the flexible foundation and rigid foundation case, the flexible foundation model predicted zero damage and the rigid foundation model predicted significantly more CLT damage.

7 | RECOMMENDATIONS FOR FUTURE RESEARCH

The design procedure and modeling methodology presented have limitations that should be addressed in future research. Future research is needed to determine the effects of three-dimensional rocking to determine how these rocking walls perform when rocking on their corners and if the base rocking multispring methodology accurately predicts the response. Additionally, future testing is needed to determine if adjustments need to be made during the design of modeling of rocking timber shear walls in tall buildings. The plastic hinge length used to estimate CLT crushing at the base of the wall is based on limited testing, and should also be considered in future research, specifically when instrumenting for future testing. Finally, it is recommended that modeling simplifications be explored and their impact on accurately predicting performance be assessed. This would consist of investigating the use of software common in design practice and is necessary for wider adoption of the system.

8 | SUMMARY AND CONCLUSIONS

Results from the two-story NHERI TallWood Project showed that post-tensioned CLT rocking walls can provide great seismic performance while remaining essentially damage-free. The walls were designed to meet three performance objectives: (1) immediate occupancy after SLE earthquakes, (2) limited repair after DBE earthquakes, and (3) collapse prevention after MCE_R earthquakes. To meet each of these three performance objectives, target drifts and damage criteria had to be met for the UFPs, the PT bars, and the CLT at the base of the rocking wall. The CLT walls met all design performance objectives while testing the building with fourteen ground motions, scaled to range from SLE hazard levels to 1.2 times the MCE_R level hazard. Although the wall system was essentially undamaged after testing, the foundation beams supporting the CLT wall panels experienced unexpected flexibility and permanent deformations.

This paper presented a numerical model for the CLT rocking walls in the two-story test specimen. Base rocking was modeled through distributed springs at the wall base and the contribution of foundation flexibility was included through additional springs below the base rocking springs. Overall, the model showed good agreement with the test results and offered a good prediction of the overall behavior and period. The numerical model underestimated drifts, resulting in lower PT bar forces, lower UFP deformations, and lower base uplift rotations. Additionally, the numerical model slightly overestimated compressive base rotations, indicating that the assumed foundation model was slightly too flexible. Like test results, the numerical model indicated no damage to the base of the CLT rocking walls.

Because the test structure was not designed to have a flexible foundation and because a typical building would be designed with a rigid foundation, an additional numerical model was created with a rigid foundation. A comparison of the rigid foundation numerical model and the flexible foundation numerical model showed that the differing boundary conditions had significant effects on overall specimen behavior. As expected, the rigid foundation greatly increased system stiffness, decreased the first mode period, and decreased drifts. Although drifts decreased, the increased stiffness due to movement of the uplift point closer to the compression toe of the wall panels resulted in larger PT bar forces relative to those observed in the test and predicted using the flexible foundation model. Most importantly, the compressive rotations at the base of the wall panels decreased significantly without the foundation beam flexibility, resulting in much higher CLT strains at the base of the wall. Under the rigid foundation boundary condition, the CLT experienced permanent yielding and damage. Thus, it is concluded that even though the flexible foundation beam produced larger peak drifts relative to the rigid foundation beam model, in general, that deformation protected the base of the wall from damage and resulted in better overall performance in terms of CLT damage.

The test specimen easily met all performance objectives and performed much better than expected. Apart from reduced roof drifts, the numerical model with the rigid foundation did not perform quite as well as it predicted considerable CLT damage in the DBE and MCE_R ground motions; however, it still predicted the system would meet all design performance objectives and the predicted performance was closer to the design intent. Because of the accurate prediction of overall building performance between test results and the flexible foundation model results, the modeling approaches presented here can be used as a good prediction for mass timber rocking wall systems.

ACKNOWLEDGEMENTS

Financial support for this study was provided by the National Science Foundation through grant CMMI 1635227, 1634628 and 1634204. Any opinions, findings, conclusions, and recommendations presented in this paper are those of the authors and do not necessarily reflect the views of the sponsors.

DATA AVAILABILITY STATEMENT

The data that support the findings of this study are openly available in DesignSafe at https://doi.org//10.17603/ds2-zcb9-ry11, reference number PRJ-1717

ORCID

Sarah Wichman https://orcid.org/0000-0003-0393-379X
Shiling Pei https://orcid.org/0000-0002-6458-3124

REFERENCES

1. Iqbal A. Seismic Response of Subassemblies for Multi-Storey Prestressed Timber buildings. Phd. Thesis. University of Canterbury, Christchurch, New Zealand; 2011.

- Sarti F. Seismic Design of Low-Damage Post-Tensioned Timber Wall Systems. Phd. Thesis. University of Canterbury, Christchurch, New Zealand; 2015.
- 3. Pei S, Huang D, Berman J, Wichman S. A simplified model for dynamic response prediction of post-tensioned cross laminated timber rocking walls. *Earthquake Eng Struct Dyn.* 2020;50:845-862.
- 4. Ganey R. Seismic design and testing of rocking cross laminated timber walls. M.S. thesis. University of Washington, Seattle, WA; 2015.
- 5. Pei S, van de Lindt JW, Barbosa AR, et al. Experimental seismic response of a resilient 2-story mass-timber building with post-tensioned rocking walls. *J Struct Eng.* 2019. http://doi.org/10.1061/(ASCE)ST.1943-541X.0002382.
- 6. Van Den Einde L, Conte JP, Restrepo JI, et al. NHERI@UC San Diego 6-DOF large high-performance outdoor shake table facility. *Front Built Environ*. 2021;6:580333. http://doi.org/10.3389/fbuil.2020.580333.
- 7. Barbosa AR, Rodrigues LG, Arijit S, et al. Shake-table experimental testing and performance of topped and untopped cross-laminated timber diaphragms. *J Struct Eng.* 2021;147(4):04021211.
- 8. Akbas T, Sause R, Ricles JM, et al. Analytical and experimental lateral-load response of self-centering posttensioned clt walls. *J Struct Eng.* 2017;143(6):04017019.
- 9. Baird A, Smith T, Palermo A, Pampanin S, (2014). Experimental and numerical Study of U-shape Flexural Plate (UFP) dissipaters. NZSEE Conference.
- Barbosa AR, Sinha A, Higgins C, Soti R, (2018). Structural Testing for the DR Johnson's CLT Panels. Report No. 17-03, Oregon State University.
- 11. Ganey R, Berman J, Akbas T, et al. Experimental investigation of self-centering cross laminated timber walls. *J Struct Eng.* 2017;143(10):04017135.
- 12. AWC. National Design Specification for Wood Construction. American Wood Council; 2015.
- 13. ASCE. Minimum design loads for buildings and other structures, ASCE/SEI 7-10, American Society of Civil Engineers; 2010.
- 14. Pampanin S, Priestley MJN, Sritharan S. Analytical modeling of the seismic behavior of precast concrete frames designed with ductile connections. *J Earthquake Eng.* 2001;5(3):329-367.
- 15. Newcombe MP, Pampanin S, Buchanan A, Palermo A. Section analysis and cyclic behavior of post-tensioned jointed ductile connections for multi-story timber buildings. *J Earthquake Eng.* 2008;12(1):83-110.
- 16. Christopoulos C, Filiatrault A, Folz B. Seismic response of self-centering hysteretic SDOF systems. *Earthquake Eng Struct Dyn.* 2002;31:1131-1150.
- 17. Seo CY, Sause R. Ductility demands on self-centering systems under earthquake loading. ACI Struc J. 2005;102(2):275-285.
- 18. Zimmerman R, McDonnel E. Framework innovation in re-centering mass timber wall buildings. Proceedings of the 11th National Conference in Earthquake Engineering. Earthquake Engineering Research Institute, Los Angeles, CA; 2018.
- 19. PEER. PEER NGA Database. Pacific Earthquake Engineering Research Center, University of California, Berkeley, California; 2006.
- 20. Mazzoni S, McKenna F, Scott M, Fenves G. Open Systems for Earthquake Engineering Simulation User Command-Language Manual OpenSees version 2.0. Pacific Earthquake Engineering Research Center, University of California, Berkeley, CA; 2009.
- 21. Kelly JM, Skiner RI, Heine AJ. Mechanisms of energy absorption in special devices for use in earthquake resistant structures. *Bull N Z Soc Earthq Eng.* 1972;5(3):63-88.
- 22. Spieth HA, Carr AJ, Pampanin S, Murahidy AG, Mander J. Modeling of precast prestressed concrete from structures with rocking beam-column connections. Report No. 2004-01, University of Canterbury, Christchurch, New Zealand; 2004.
- 23. Hasani H, Ryan KL, Wichman S, Berman J. Dynamic behavior of mass timber building with cross-laminated timber rocking walls. *Earthq Eng Struct Dyn.* 2021. In Press.
- 24. Wichman S. Large-scale dynamic testing of rocking cross laminated timber walls. M.S. thesis. University of Washington, Seattle, WA; 2018.

How to cite this article: Wichman S, Berman JW, Pei S. Experimental investigation and numerical modeling of rocking cross laminated timber walls on a flexible foundation. *Earthquake Engng Struct Dyn.* 2022; 1–21. https://doi.org/10.1002/eqe.3634